


Article

Airborne Hyperspectral Evaluation of Maximum Gross Photosynthesis, Gravimetric Water Content, and CO₂ Uptake Efficiency of the Mer Bleue Ombrotrophic Peatland

J. Pablo Arroyo-Mora ^{1,*} , Margaret Kalacska ^{2,3}, Raymond J. Soffer ¹, Tim R. Moore ³, Nigel T. Roulet ³, Sari Juutinen ⁴, Gabriela Ifimov ¹, George Leblanc ^{1,3} and Deep Inamdar ^{2,3}

¹ Flight Research Laboratory, National Research Council of Canada, Ottawa, ON K1A-0R6, Canada; raymond.soffer@nrc-cnrc.gc.ca (R.J.S.); gabriela.ifimov@nrc-cnrc.gc.ca (G.I.); george.leblanc@nrc-cnrc.gc.ca (G.L.)

² Applied Remote Sensing Lab., McGill University, Montreal, QC H3A-0B9, Canada; margaret.kalacska@mcgill.ca (M.K.); deep.inamdar@mail.mcgill.ca (D.I.)

³ Department of Geography, McGill University, Montreal, QC H3A-0B9, Canada; tim.moore@mcgill.ca (T.R.M.); nigel.roulet@mcgill.ca (N.T.R.)

⁴ Environmental Change Research Unit (ECRU), Ecosystems and Environment Research Programme, Faculty of Biological and Environmental Sciences, University of Helsinki, P.O. Box 65, 00014 Helsinki, Finland; sari.juutinen@helsinki.fi

* Correspondence: JuanPablo.Arroyo-Mora@nrc-cnrc.gc.ca; Tel.: +1-613-993-7296

Received: 19 February 2018; Accepted: 4 April 2018; Published: 6 April 2018



Abstract: Peatlands cover a large area in Canada and globally (12% and 3% of the landmass, respectively). These ecosystems play an important role in climate regulation through the sequestration of carbon dioxide from, and the release of methane to, the atmosphere. Monitoring approaches, required to understand the response of peatlands to climate change at large spatial scales, are challenged by their unique vegetation characteristics, intrinsic hydrological complexity, and rapid changes over short periods of time (e.g., seasonality). In this study, we demonstrate the use of multitemporal, high spatial resolution (1 m²) hyperspectral airborne imagery (Compact Airborne Spectrographic Imager (CASI) and Shortwave Airborne Spectrographic Imager (SASI) sensors) for assessing maximum instantaneous gross photosynthesis (PG_{max}) in hummocks, and gravimetric water content (GWC) and carbon uptake efficiency in hollows, at the Mer Bleue ombrotrophic bog. We applied empirical models (i.e., in situ data and spectral indices) and we derived spatial and temporal trends for the aforementioned variables. Our findings revealed the distribution of hummocks (51.2%), hollows (12.7%), and tree cover (33.6%), which is the first high spatial resolution map of this nature at Mer Bleue. For hummocks, we found growing season PG_{max} values between 8 μmol m⁻² s⁻¹ and 12 μmol m⁻² s⁻¹ were predominant (86.3% of the total area). For hollows, our results revealed, for the first time, the spatial heterogeneity and seasonal trends for gravimetric water content and carbon uptake efficiency for the whole bog.

Keywords: airborne hyperspectral; Compact Airborne Spectrographic Imager (CASI); Shortwave Airborne Spectrographic Imager (SASI); peatlands; normalized difference water index (NDWI); gravimetric water content; carbon uptake; photosynthesis; bog; Mer Bleue

1. Introduction

Peatlands are characterized by the accumulation of large amounts of organic carbon (C), generally from 30 kg C m⁻² to >250 kg C m⁻² [1]. This accumulation derives from the imbalance between

the input of plant production and the output of C as carbon dioxide, methane and dissolved and particulate organic carbon. Long-term C accumulation rates of $10\text{--}50\text{ g C m}^{-2}\text{ year}^{-1}$ are common in northern peatlands, which store more than 400 Gt C [1]. Northern peatlands are often characterized by a spatial patterning of the vegetation and microforms, which can be regular or irregular and have a small scale (1–10 m) [2,3]. In bogs, which are nutrient-poor peatland complexes with a convex surface, the microforms are called hummocks and hollows, lawns being the intermediate surface in between. Hummocks are drier elevated mounds with a denser cover of vascular plants and a thicker acrotelm (aerated layer above the water table) than lower-lying, wetter hollows, which are dominated by mosses (in bogs, generally *Sphagnum* spp.) [2,3]. These two microforms differ in species composition and rates of processes such as photosynthesis and respiration [3,4]. Usually, the vertical microtopographic variation between hummocks and hollows is much less than 1 m [5].

Hydrology plays an important role in the C functioning of peatlands. A high water table slows the rate at which organic matter decomposes (e.g., [6]). A high water table also constrains the growth of many vascular plants, whose roots are unable to penetrate beneath the water table, thereby restricting their effective rooting volume to the aerobic surface layer (e.g., [7]). Vascular plant production generally increases with a lowering of the water table (e.g., [8]). In many northern peatlands, *Sphagnum* species play a critical role in the accumulation of C, through their slow rates of decomposition, compared to vascular plant tissues (e.g., [6,9]). Their absence of roots means they can tolerate the high water table common in peatlands and they generate an environment favourable to their survival (e.g., [10]). *Sphagnum* productivity is also influenced by the moisture content at the surface, with many studies having shown that the photosynthetic and C uptake rates of *Sphagnum* species are dependent on the moisture content of the capitulum (e.g., [11,12]). As the moisture content increases, the rate of CO₂ uptake increases until an optimum value is reached (generally between 700% and 1300% gravimetric moisture content) and then decreases as the *Sphagnum* gets wetter. Severe desiccation reduces photosynthesis, with a potentially long recovery period after re-wetting (e.g., [13]). *Sphagnum* survives drying by developing a dense structure, which reduces moisture loss such as in hummock species, or by retaining contact with the water table through a high capillarity, such as in hollow species.

Mapping the spatial and temporal variations in surface moisture content and water-table position in peatlands is critical for assessing the C functioning of these ecosystems. To map the spatial variability of these characteristics through time, remote-sensing approaches require high spatial and spectral resolutions and an adequate temporal interval of imagery acquisition (e.g., intra- and inter-seasonal). Hydrological studies considering near-surface water content and water-table position in peatlands have shown the potential of hyperspectral data for assessing water stress in *Sphagnum* mosses [14,15] as well as in the implementation of upscaling approaches [16,17]. *Sphagnum* mosses have different spectral properties than vascular plants. In the visible region of the electromagnetic spectrum, mosses present a “green” peak that depends on species the color (e.g., red, brown, or green) [18]. In addition, [19] found that *Sphagnum* mosses had lower reflectance than typical green vegetation between 1.3 μm and 2.4 μm . Water-related absorption features around 1 μm and 1.2 μm are also noticeable in *Sphagnum* mosses and they are highly susceptible to desiccation [19]. Narrowband spectral indices in the shortwave infrared (SWIR) region of the electromagnetic spectrum (e.g., normalized difference water index NDWI₁₆₄₀) and continuous wavelet transforms have been successfully used to evaluate near-surface water content which is related to the water-table position [14–17,20]. Given the high spatial variability of peatland microtopography [21], pixel sizes no larger than 1 m are necessary to adequately map surface-water variations. Furthermore, [16] indicates the need for quantitative hydrological information for entire peatland complexes, which is quite challenging as hyperspectral airborne missions for entire complexes are expensive and rarely span the intra- and inter-seasonality of peatland areas. Another challenging aspect in assessing moisture in peatlands is that vascular plants are physiologically distinct from mosses [10] and, therefore, modeling moisture-related variables (e.g., gravimetric water, water-table relationships, photosynthetic efficiency) at the landscape level needs to consider the spatial patterns of the vascular and non-vascular plants (e.g., mosses).

In this study we applied empirical models to high spatial resolution (1 m) hyperspectral imagery (HSI) to map biophysical variables related to C dynamics [13,22] at the Mer Bleue Conservation Area, which is an ombrotrophic bog near Ottawa, ON, Canada. We first produced a map of microforms (i.e., hummocks and hollows) and trees for Mer Bleue from visible-near infrared (VISNIR) HSI (Compact Airborne Spectrographic Imager (CASI) sensor) [23] and LiDAR data. From this classification, we modeled vascular plant-light saturated gross photosynthesis (PG_{max}) based on a CASI HSI dataset from 23 June 2016. For hollows (i.e., exposed *Sphagnum* sp.), we used SWIR HSI imagery (Shortwave Airborne Spectrographic Imager (SASI) sensor) [23] to derive near-surface moisture, gravimetric water content and C uptake efficiency (i.e., relative net rate of CO₂ uptake [13]) over 5 periods. Because Mer Bleue is an Arctic Surrogate Simulation Site for Sentinel-2 and Landsat-8 satellite product validation [24,25], our findings have the potential to inform satellite image analysis for modeling C uptake efficiency at large spatial scales (e.g., >100 ha). Furthermore, this research contributes to highlighting the necessity of including peatlands in global models as recently demonstrated by [26].

2. Materials and Methods

2.1. Study Area

The 35 km² Mer Bleue Conservation Area (MBCA) located approximately 10 km east of Ottawa, ON, Canada, includes an ombrotrophic bog that is representative of northern peatlands in terms of its C budget (Figure 1A) [27]. Ombrotrophic peatlands are acidic, nutrient-poor ecosystems that receive incoming water and nutrients from precipitation and deposition rather than telluric sources [28]. Vegetation at Mer Bleue has been extensively described in terms of species composition and structural characteristics [29–31]. Overall, Mer Bleue is characterized by hummock-hollow-lawn microtopographic features, treed bog areas, poor fen sections, and a relatively dense mixed forest in the middle. The mean relief between hummocks and hollows is less than 30 cm and the variable water table is generally below the surface even for the hollows [32]. Mer Bleue also contains continuously inundated beaver ponds around its margins, with open water and areas covered mainly by cattail (*Typha angustifolia*) and floating *Sphagnum* (Figure 1B,C). Vegetation in the MBCA encompasses evergreen and deciduous shrubs (*Chamaedaphne calyculata*, *Rhododendron groenlandicum*, *Kalmia angustifolia*, *Vaccinium myrtilloides*), patches of sedges (*Eriophorum vaginatum*) and a few isolated individuals and patches of *Picea mariana*, *Betula populifolia* and *Larix laricina*. Different species of *Sphagnum* moss (*S. capillifolium*, *S. fuscum*, *S. magellanicum*) cover the surface of the bog [32] and are exposed in the hollows, while the vascular plants comprise the upper plant canopy in hummocks [27]. Mer Bleue has a cool continental climate, with a mean annual temperature of 6.4 °C and a mean annual precipitation of 943.4 mm (Canadian Climate Normals 1981–2010). According to [7], the average growing season length is 182 days beginning in mid-April and ending in mid-October. For this study we focused on a 19 km² section of Mer Bleue which was primarily composed of the peatland without the surrounding mineral soil treed areas (Figure 1A).

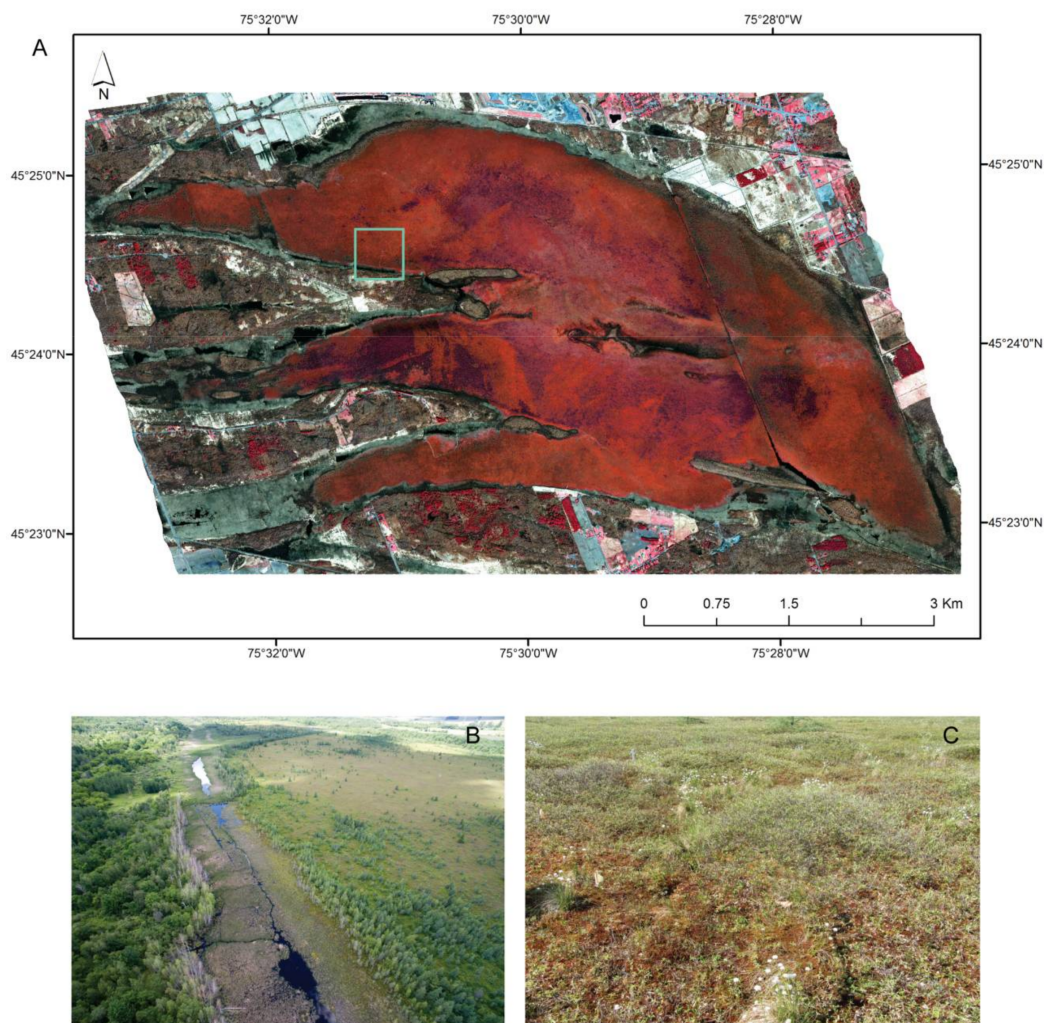


Figure 1. (A) CASI hyperspectral image mosaic of 12 flight lines acquired 20 April 2016 (R: 756 nm, G: 689 nm, B: 550 nm) illustrating the entire study area. The green box corresponds to the Mer Bleue Peatland Observatory where most of the in situ research is carried out. (B) Unmanned aerial vehicle (UAV) photograph of the peatland margin illustrating a beaver pond with open water, *Typha angustifolia* and floating *Sphagnum* moss. The peatland can be seen to the right (north) of the beaver pond with mixed forest on mineral soil to the left (south); (C) Ground photograph illustrating the small-scale (<50 cm) hummock-hollow microtopography. Brown-red areas correspond to moss vegetation in hollows, and green areas correspond to vascular plants in hummocks.

2.2. Airborne Hyperspectral Imagery (HSI)

The airborne HSI mission was part of a multitemporal satellite product validation project [24], where HSI data were acquired over multiple dates between November 2015 and June 2016. A Compact Airborne Spectrographic Imager 1500 (CASI-1500) and a Shortwave Airborne Spectrographic Imager (SASI-644) (ITRES Ltd., Calgary, AB, Canada), mounted on a Twin Otter aircraft, were used for HSI acquisition. The CASI samples 288 spectral channels between 375 nm and 1054 nm, with 1498 across track pixels, and a field of view of 39.9°. The SASI samples 160 spectral channels from 883 nm to 2523 nm, with 640 across track pixels, and a field of view of 39.7° (Table 1). In this study, we used one CASI dataset from 23 June 2016 to differentiate hollows and hummocks and estimate the maximum gross photosynthesis (PGmax) for hummocks (Section 2.5). Five SASI datasets (Table 2) were used to assess changes in near-surface moisture, gravimetric water content and C uptake for *Sphagnum* mosses (Section 2.6).

Table 1. Summary of the Compact Airborne Spectrographic Imager (CASI-1500) and Shortwave Airborne Spectrographic Imager (SASI-644) characteristics.

Characteristic	CASI-1500	SASI-644
Serial Number	2511	3102
Field of view (FOV) (°)	39.9°	39.7°
Instantaneous FOV (IFOV) (°)	0.0270 (nadir) 0.0246 (edge)	0.0646 (nadir) 0.0572 (edge)
No. cross-track pixels (detector)	1500	644
No. cross-track pixels (image)	1498	640
No. channels	288 (max)	160
Spectral range (nm)	375–1054	883–2523
Spectral spacing (nm)	2.4	10.0 nm @ 883 nm 12.8 nm @ 1280 nm (max) 6.2 nm @ 2523 nm
Spectral resolution (nm)	3.2	16 nm @ 883 nm 12 nm @ 2523 nm
Frame rate (Frames s ^{−1})	Programmable—Max rate dependent on # of channels	60 Hz
Integration time (IT) (ms)	1000/Frame rate	<16.67 (Typ. 2.0–6.0)
Focal length (FL) (pixels)	2067.36	886.571

To cover the entire MBCA, 12 flight lines with a 20% overlap were acquired with both instruments, with the exception of 4 November 2015 with 9 flight lines. Flight data acquisition parameters used for each date are shown in Table 2.

Table 2. Flight heading and illumination characteristics for the 5 image-acquisition dates. All flights were conducted at an approximate altitude of 1000 m AGL.

Date	Heading (°)	Sun Azimuth Angle (°) Range	Sun Zenith Angle (°) Range
4 November 2015	344.9 ± 1.0	170.2–191.6	61.1–62.0
20 April 2016	345.9 ± 1.0	153.6–180.3	33.6–36.9
11 May 2016	341.7 ± 0.8	137.6–178.0	27.3–33.8
24 May 2016	340.1 ± 1.5	139.2–189.6	24.7–29.6
23 June 2016	338.8 ± 0.5	128.6–157.9	23.3–30.0

2.3. Hyperspectral Imagery Pre-Processing

For the five mosaic dates, the individual CASI and SASI flight-line images were spectroradiometrically calibrated to units of spectral radiance ($\mu\text{W cm}^{-2} \text{sr}^{-1} \text{nm}^{-1}$) and then geometrically corrected. These pre-processing steps were performed using software modules developed by the sensors' manufacturer. The spectroradiometric calibration was performed using a NIST traceable laboratory calibration performed on March 2015 by the instrument manufacturer. The geocorrection process was performed using results from a bundling calibration designed to relate the inertial measurement unit (a combined Global Positioning System (GPS) and inertial navigation system) to the sensor geometry in May 2016 for the CASI and in April 2013 for the SASI. The pre-processing modules include an image-based assessment and correction of the spectral alignment (*calibcorr*), a removal of signal offsets inherent in the recorded digital pixel values from sources unrelated to the image independent (electronic offset, dark current) and image-dependent (frame shift smear, scattered light, and 2nd order diffracted light (CASI only)) sources; spectroradiometric calibration routine (*radcorr*); a spectral-smile correction application (*speccorr*); and an

image geocorrection routine (*geocorr*). Our mosaic approach made use of the ‘minimize view zenith angle’ option to select which of the duplicate pixels located in the overlap area between flight lines are applied in the resulting mosaic imagery.

Mission planning not only attempted to acquire the hyperspectral image flight lines as coincidental as possible with the Sentinel-2 satellite overpass [24], but also at a planned ground-track designed to optimize the alignment with respect to the solar azimuth angle (SAA) to minimize potential cross-track illumination effects (Table 2). Due to the length of the data-acquisition process which took approximately 1.5 h to acquire the 12 flight lines, cross-track illumination artifacts were evident along the flight-line seams within the hyperspectral mosaics, increasing in intensity, as expected, as the difference of the sensor heading with respect to the SAA increased (sensor heading is equal to the ground track less the crab angle) [33]. To address this issue, a first order cross-track illumination correction routine as implemented in ENVI 5.4.1 was applied to the individual flight-line radiance images prior to geocorrection to reduce the impact of this artifact. This resulted in final mosaic products in which there is minimal to no illumination artifacts apparent along the flight-line seams. Still, some illumination artifacts remained in a few areas of the mosaics, although given the large area under analysis, we considered the effects of these artifacts on the results would be minimal.

For the SASI imagery, the atmospheric correction was performed to the resulting mosaic with the FLAASH module in the ENVI 5.4.1. For the single CASI mosaic, atmospheric correction was applied to the individual flight lines using ATCOR4 4.7.0 for flat terrain [30] prior to the application of the cross-track illumination correction and image mosaicking.

2.4. Hummock and Hollow Classification

2.4.1. Plant Area Index In Situ Empirical Model

Plant area index (PAI) (vascular plant area between ground and sky) was determined with a LI-COR 2000 for 29 field plots (44 cm × 44 cm) during the week of 13–15 July 2009 along a transect spanning the main research boardwalks in the MBCA including a range of vegetation microforms (hummock, lawns, hollows). We measured the reflectance ratio over the 400–1100 nm range of the plots using an ASD Handheld spectrometer with a bare fibre 25° field of view (Analytical Spectral Devices, Boulder, CO, USA) under clear skies on 14 July. PAI was related to the photochemical reflectance index (PRI) [34,35] where ρ_{531} is the reflectance at 531 nm and ρ_{570} is the reflectance at 570 nm (Equation (1), Figure 2). The PAI:PRI function (Figure 2) was applied to the observed PRI derived from the CASI mosaic from 23 June to estimate PAI for the entire study area. The PAI surface was also used to identify trees and aid in the differentiation of hummocks and hollows (Sections 2.4.2 and 2.4.3).

$$\text{PRI} = \frac{\rho_{531} - \rho_{570}}{\rho_{531} + \rho_{570}} \quad (1)$$

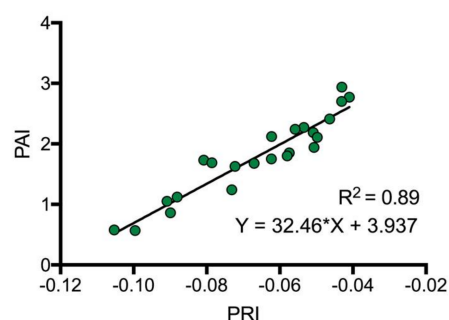


Figure 2. Relationship between the photochemical reflectance index (PRI) and plant area index (PAI) ($p < 0.0001$).

2.4.2. Tree Mask

Airborne full waveform LiDAR data collected for the National Capital Commission in November 2009 (absolute accuracy of 15 cm vertical and 50 cm horizontal, minimum density 2 pts m⁻²) were available for two thirds of the study area. From the LiDAR, we defined trees as vegetation >30 cm tall and with a canopy diameter >30 cm. However, because the south-eastern sector of the MBCA was LiDAR data deficient we used the existing LiDAR to develop a model using the CASI PAI surface to extract “trees” in a consistent way for the entire study area. We determined a PAI threshold for trees (and dense vascular vegetation such as tall shrubs) from the full CASI mosaic from 23 June (Section 2.4.1) so that PAI values greater than 2.0 corresponded to dense vegetation at the 1 m pixel size of the CASI (Figure 3).

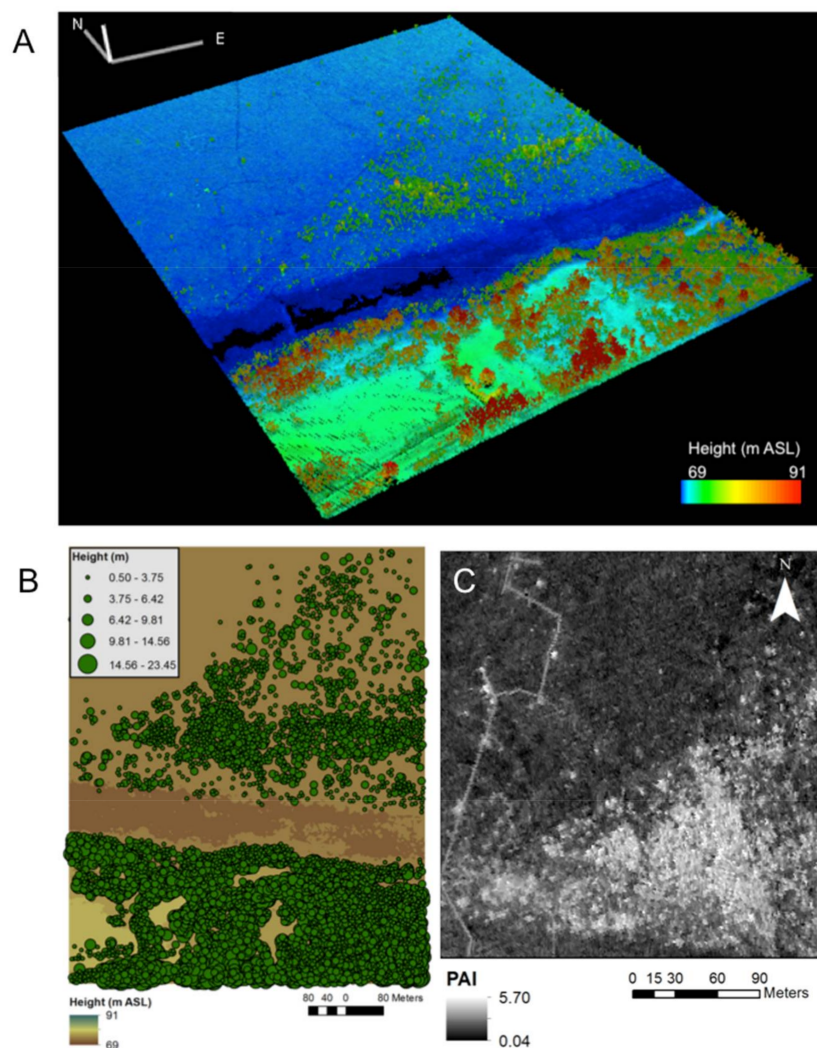


Figure 3. (A) Example of the LiDAR point cloud for the research boardwalk area of the Mer Bleue Conservation Area (MBCA); (B) digital surface model from the LiDAR (basemap) with points representing trees >30 cm in canopy diameter and height (green points); (C) PAI surface derived from the CASI mosaic.

2.4.3. Hummock and Hollow Differentiation

A high-resolution (2.2 cm ground-sampling distance) digital surface model (DSM) of the research boardwalk area, generated from unmanned aerial vehicle (UAV)-based photogrammetry as described in [21], was used to determine the threshold in PAI between hummocks and hollows from the CASI

PAI surface. Hollows were determined to be the lowest 25% of the elevation distribution from the UAV–DSM [36]. By applying this height threshold from the UAV–DSM to the PAI surface, we determined that hollows were represented by pixels with a PAI < 0.96. In addition, because hollows can be smaller than 1 m² and the PAI surface was generated in the leaf-on period (vascular plants), the reflectance ratio between 883 nm and 1240 nm was examined. It was shown by [24] that for hummocks the ratio is negative from both vascular plant leaf-on and leaf-off periods while for hollows it is positive. Therefore, hummocks were determined to be areas with a PAI between 0.96 and 2.0 and a negative reflectance ratio of 883 nm to 1240 nm from SASI imagery acquired on 20 April (leaf off) and 23 June (leaf on). Hollows were determined to be areas with a PAI between 0 and 0.96 and a positive reflectance ratio (ρ_{883}/ρ_{1240}) from both April and June.

2.5. Vascular Plant (Hummocks) Light-Saturated Gross Photosynthesis (PG_{max})

Ecosystem CO₂ exchange was measured in 15 primarily hummock plots during four sampling periods from July–August 2009. Paired measurements of net ecosystem exchange under light-saturated conditions, i.e., photosynthetically active photon flux density >1000 $\mu\text{mol photons m}^{-2} \text{s}^{-1}$, and dark respiration of CO₂, were conducted using a Plexan chamber (60 cm × 60 cm × 90 cm) equipped with fans and cooling unit. The chamber was covered with an opaque hood for measuring the ecosystem dark respiration. CO₂ concentrations over the time of chamber closure were analyzed using a LiCOR 6200 infrared analyzer. Fluxes of CO₂ were calculated on the basis of concentration change in the chamber head space as a function of time. Fluxes were corrected for temperature and atmospheric pressure. Light-saturated gross photosynthesis (PG_{max}) was calculated as the sum of net exchange and dark respiration [22,37]. Coincident with the measurements of CO₂ flux, field spectra representing the reflectance ratio were collected with the ASD Handheld spectrometer (bare fibre 25° field of view). The normalized difference vegetation index (NDVI) (Equation (2)) was calculated from the field spectra:

$$\text{NDVI} = \frac{\rho_{\text{NIR}} - \rho_{\text{Red}}}{\rho_{\text{NIR}} + \rho_{\text{Red}}} \quad (2)$$

where ρ_{NIR} and ρ_{Red} are the reflectance at 860 nm and 650 nm from the spectroradiometer respectively. NDVI was related to PG_{max} via the relationship in Figure 4.

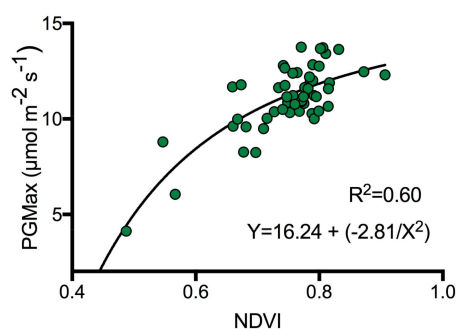


Figure 4. Relationship between normalized difference vegetation index (NDVI) and PG_{max} ($\mu\text{mol m}^{-2} \text{s}^{-1}$) for 15 plots over four sampling dates (July–August 2009).

The function identified in Figure 4 relating NDVI and PG_{max} was applied to the NDVI surface calculated from the 23 June CASI HSI mosaic with ρ_{NIR} as 859.39 nm and ρ_{Red} as 649.02 nm. Four broad classes of PG_{max} (<4, 4–8, 8–12, >12 $\mu\text{mol m}^{-2} \text{s}^{-1}$) for the hummocks were inferred from [22].

2.6. Near-Surface Moisture, Gravimetric Water Content, and CO₂ Uptake Efficiency (Hollows)

Because gravimetric water (GWC) content and CO₂ uptake efficiency were assessed by [13,17] for *Sphagnum* moss, we limit our analysis for these two variables to hollows (i.e., mosses are exposed).

Therefore, in order to assess the temporal changes in gravimetric water content and CO₂ uptake efficiency for the hollows from the five SASI mosaics, we first calculated the near-surface moisture content based on the normalized difference water index (NDWI₁₆₄₀, Equation (3)) [38].

$$\text{NDWI}_{1640} = \frac{\rho_{883} - \rho_{1640}}{\rho_{883} + \rho_{1640}} \quad (3)$$

where ρ_{883} is the reflectance at 883 nm and ρ_{1647} is the reflectance at 1640 nm [21]. Then, from the NDWI₁₆₄₀ we derived gravimetric water (GWC) content for the hollows based on an empirical relationship found by [17] (Equation (4)) and previously tested for a section of the MBCA by [21].

$$\text{GWC} = 4714 \times \text{NDWI}_{1640} + 437.7 \quad (4)$$

For the hollows, four classes of CO₂ uptake efficiency based on GWC were inferred from [13]. These four classes included GWC up to 250% which was shown by [13] to be water-deficient conditions where *Sphagnum* is only functioning at a maximum of 20% capacity of CO₂ uptake; 250–700% which represent sub-optimal moisture conditions where *Sphagnum* is functioning up to 80% of its maximum capacity of CO₂ uptake; 700–1300% which represent optimal conditions for CO₂ uptake; and >1300% which represent wet conditions approaching saturation where CO₂ uptake is reduced.

3. Results

We found that hummocks cover 51.2% of the total area, hollows 12.7% and trees 33.6% (Figure 5). Unclassified vegetation and water account for only a small portion of the Mer Bleue peatland (2.4%). The spatial distribution of PGmax from 23 June 2016 for the hummocks is shown in Figure 6. PGmax values between 8 and 12 ($\mu\text{mol m}^{-2} \text{s}^{-1}$) comprise 86.3% of the area and are distributed throughout the bog, with the exception of the middle section of the peatland where PGmax values between 4 and 8 ($\mu\text{mol m}^{-2} \text{s}^{-1}$) cover 9.9% of the area.

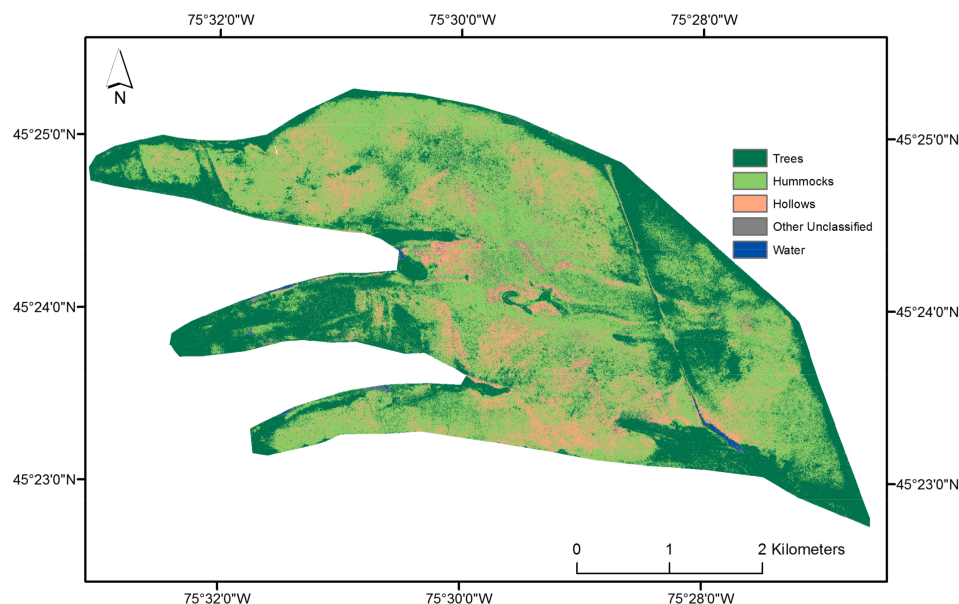


Figure 5. Distribution of peatland microform and tree classes for Mer Bleue based on CASI imagery from 23 June 2016.

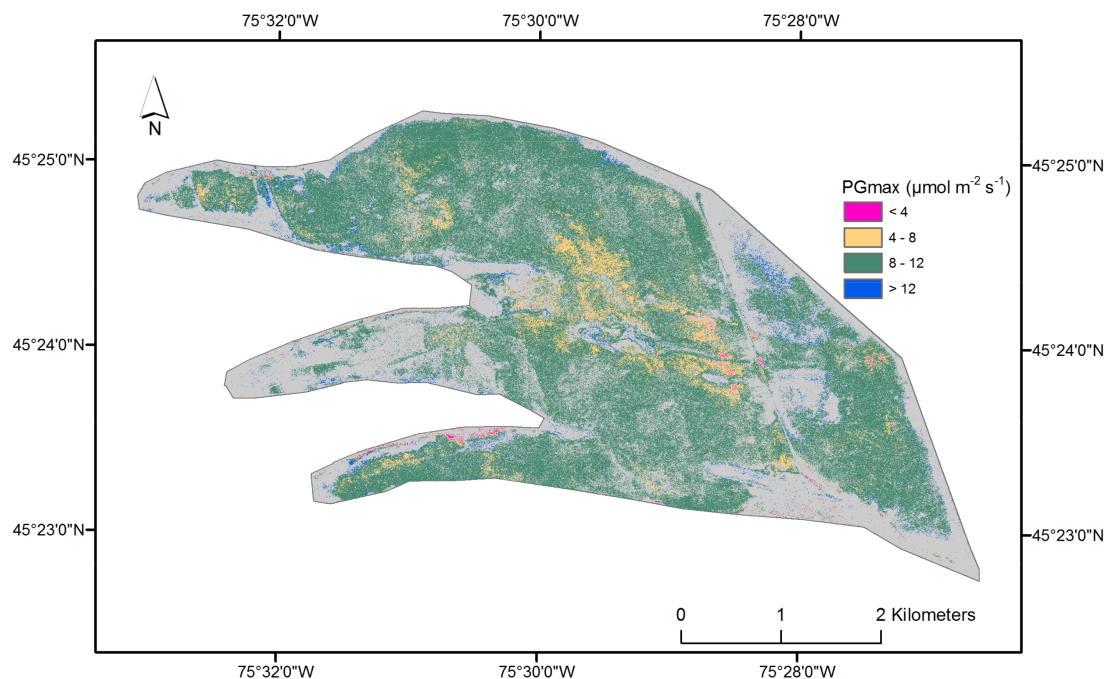


Figure 6. Spatial distribution of maximum gross photosynthesis (PGmax) for hummock surfaces at Mer Bleue based on CASI imagery from 23 June 2016. Areas in grey include hollows and treed areas not included in the PGmax analysis.

NDWI₁₆₄₀ spectral index results reveal a decreasing trend from 4 November 2015 (HO: 0.181, HU: 0.110) to 4 April 2016 (HO: 0.151, HU: 0.076) for both hollows and hummocks (Table 3, Figure 7). From 4 April 2016 to 11 May 2016, NDWI₁₆₄₀ values are similar, and there is a slight decrease in near-surface moisture for hollows and hummocks from 11 to 24 May 2016 (Table 3, Figure 7). Then, near-surface moisture content increases for 23 June 2016 (HO: 0.174 and HU: 0.174) to values similar to hollows in 5 November 2015 (0.181) (Table 3, Figure 7). Overall, hollows have higher near-surface moisture values than hummocks with the exception of 23 June 2016 (Table 3, Figure 8). *t*-test results comparing hollows and hummocks for each date indicates a significant difference between these vegetation types ($p = 0$, $\alpha = 0.05$) (Table 3). Because of the large sample size used in the *t*-test we also calculated the probability density functions (PDF) comparing hollow (HO) versus hummock (HU) near surface water content based on the NDWI₁₆₄₀ (Figure A1 and Table A1). Overall, PDF results indicate a greater NDWI₁₆₄₀ in hollows than in hummocks.

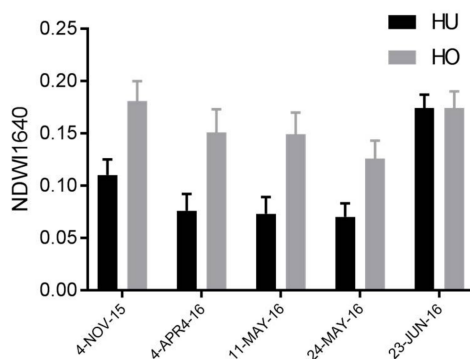


Figure 7. Hollows' and hummocks' near-surface moisture temporal trends for five time periods based on NDWI₁₆₄₀ (SASI HSI) at the Mer Bleue bog (mean and standard deviation).

Table 3. Mean, standard deviation and *t*-test statistics for paired *t*-test comparison results of NDWI₁₆₄₀ spectral index (near-surface water content) for hollows (HO) and hummocks (HU) for five dates at the MB bog.

	Mean	Stdev	tstat	df	sd	ci	<i>p</i> -Value
4 November 2015							
HO ($n = 2.40 \times 10^6$)	0.181	0.181	−1104.05	3,838,142	0.0907, 0.0868	−0.0701, −0.0699	0
HU ($n = 9.41 \times 10^6$)	0.110	0.015					
20 April 2016							
HO ($n = 2.43 \times 10^6$)	0.151	0.022	−1123.08	3,647,862	0.0895, 0.0925	−0.0741, −0.0738	0
HU ($n = 9.77 \times 10^6$)	0.076	0.016					
11 May 2016							
HO ($n = 2.43 \times 10^6$)	0.149	0.021	−1169.98	3,689,468	0.0894, 0.0908	−0.0760, −0.0758	0
HU ($n = 9.77 \times 10^6$)	0.073	0.016					
24 May 2016							
HO ($n = 2.43 \times 10^6$)	0.126	0.017	−1023.25	3,484,644	0.0832, 0.0919	−0.0663, −0.0661	0
HU ($n = 9.77 \times 10^6$)	0.070	0.013					
23 June 2016							
HO ($n = 2.43 \times 10^6$)	0.174	0.016	−406.85	3,295,761	0.0628, 0.0763	−0.0216, −0.0214	0
HU ($n = 9.77 \times 10^6$)	0.174	0.013					

Note: tstat is value of the test statistic, df correspond to degrees of freedom, sd is the pooled estimate of the population standard deviation, and ci is the confidence interval for the difference in population means of hollows and hummocks.

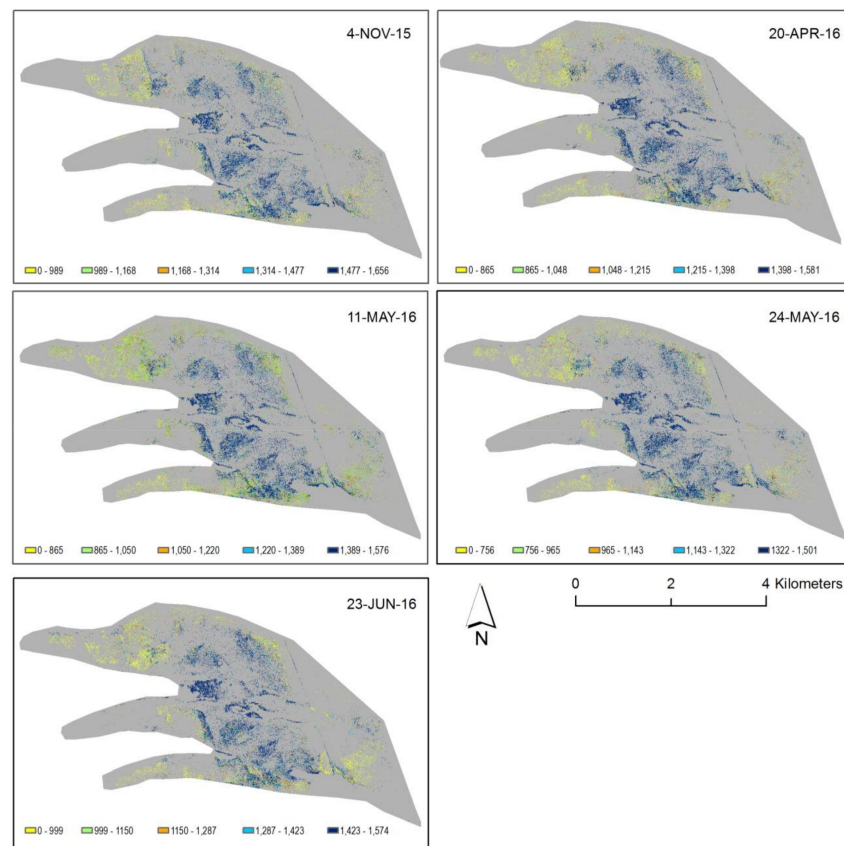


Figure 8. Spatial pattern of gravimetric water content (GWC%) in hollows at the Mer Bleue peatland for five dates between 4 November 2015 and 23 June 2016. The bins represent the natural breaks based on 5 classes; therefore, the range of each class differs slightly by date.

The GWC results for hollows reveal the spatial variations in different sections of Mer Bleue as well as in the temporal trends (Figures 8 and 9, respectively). Changes in GWC are most noticeable in the north-west portion of Mer Bleue. This portion has lower GWC following snow melt (24 April 2016) than prior to snow fall the previous year (4 November 2015). The lowest GWC values are seen from the 24 May 2016 imagery. A similar pattern is observed in the south-eastern area part of Mer Bleue. The middle area of Mer Bleue remains more or less consistent with high GWC values (e.g., >1300%). Overall GWC for hollows confirms the temporal trends expected at Mer Bleue (Figure 9A). Our analysis of variance (ANOVA) results comparing GWC between the different periods indicates significant differences for all periods ($p = 0$, $\alpha = 0.05$) (Table 4), while the Tukey's honest significant difference (HSD) tests for all pairwise comparisons between means reveal that each period is significantly different from each other (result not shown). Because of the large the sample size, as suggested by the t -test results (Table 3), the probability density functions of GWC (Figure 9B), better depict, visually, the differences in GWC between periods.

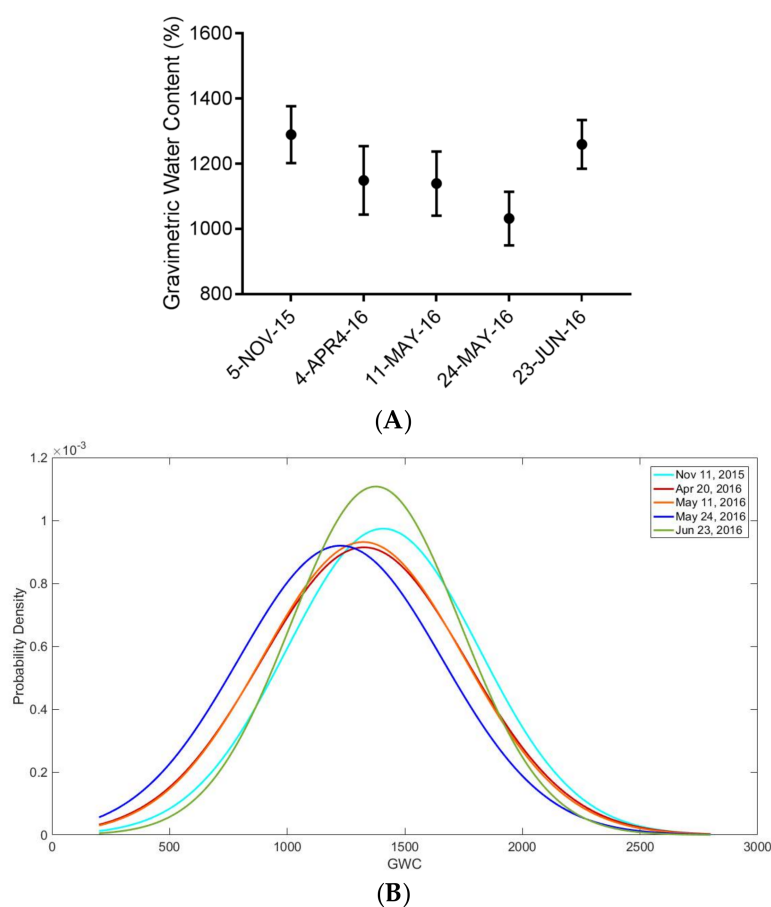


Figure 9. (A) Temporal gravimetric water content (GWC) changes for hollows at the Mer Bleue peatland (mean \pm standard deviation). (B) Probability density function for GWC for the same dates.

Table 4. Multiple group comparison for GWC at Mer Bleue for five dates between 4 November 2105 and 23 June 2016.

Source	SS	df	MS	F	Prob > F
Groups	4.6×10^{10}	4	11,469,950,111	667,178	0
Error	2.1×10^{12}	12,120,001	171,917		
Total	2.1×10^{12}	12,120,005			

Spatial patterns of CO₂ uptake efficiency in hollows derived from SASI HSI show that, regardless of the time period, the central area of Mer Blue is considered wet (>1300% GWC class) and therefore is inferred to have a lower net rate of CO₂ uptake than drier hollow areas (Figure 10). The suboptimal category (200–700% GWC) is more noticeable in the north-western part of Mer Bleue, especially in the 24 May 2016 imagery, where the suboptimal class (250–700% GWC) dominates and dry conditions also present (<250% GWC). Overall, there is a larger predominance of the wet and optimal categories; however, the overall percentage of areas defined as wet decreases by approximately 20% from 4 November 2015 to 24 May 2016 as these areas became optimum. (Figure 11). Smaller variations across time are shown in the optimal category, while the suboptimal category shows an increase of approximately 10% during the 14 May 2016 period (Figures 10 and 11).

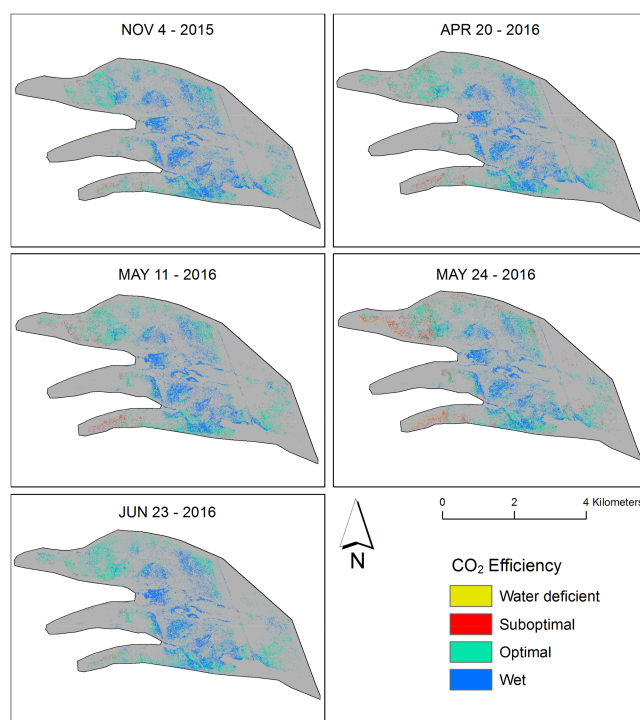


Figure 10. Spatial patterns of CO₂ uptake efficiency for hollows over five dates at the Mer Bleue peatland.

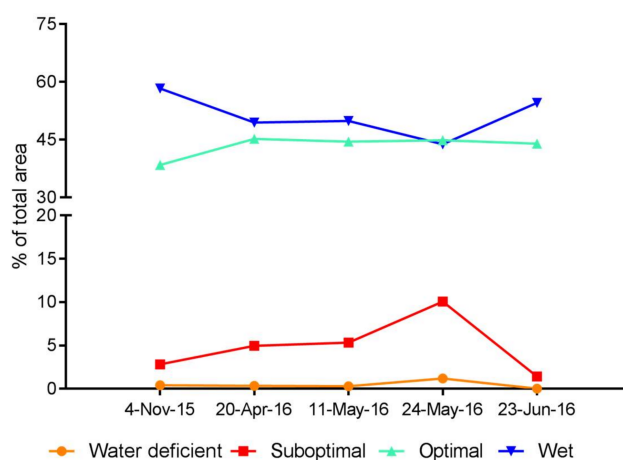


Figure 11. Percentage of total area for CO₂ uptake efficiency for hollows for five dates at the Mer Bleue peatland.

4. Discussion

Our study is the first of its kind as it integrates empirical models and multitemporal airborne hyperspectral imagery (VISNIR and SWIR) to develop estimates of the spatial variation of two C exchange parameters (ecosystem PGmax of hummock vegetation and CO₂ uptake efficiency of hollow *Sphagnum* mosses) across a large peatland with variable microtopography, vegetation and hydrology. Due to the spatial pattern of vegetation communities in peatland and its microtopographic elements [2,39], ideally the classification of vegetation microforms (e.g., vascular plant-dominated hummocks, exposed mosses in hollows, trees, etc.) in peatlands would utilize very fine spatial-resolution imagery (<1 m) (e.g., [21,40]). However, since we did not have a fine-scale elevation grid for the whole study area, we derived the relationship between PAI and PRI (Figure 2) and applied it to the CASI imagery from 23 June 2016. By determining thresholds of modeled PAI derived from the aforementioned relationship from a microtopography digital elevation model for a subset representative of Mer Bleue's microforms [32], we were able to classify hummocks (vascular plant-dominated) and hollows (exposed moss-dominated). Classification of the entire bog allowed us to determine not only the proportion of hummocks and hollows but their spatial distribution as well (Figure 5). For instance, it has been shown that the main research area located in the north-western sector of the bog (i.e., top finger) is dominated by hummocks [32]. Based on our results, hummocks represent approximately 51.2% of the total area, but the dominant microform varies spatially throughout; the centre of the bog is dominated by hollows while the north-eastern and central western sectors have a high proportion of tree cover (Figure 5). Due to the spatial resolution of the CASI imagery (1 m²), our estimation of hollows is conservative and areas with smaller hollows may have been missed (and hummocks in that region overestimated). The treed areas located on the western side of the middle of the bog are associated with areas of sandy deposits remnant from the formation of the bog 8500 years B.P. [32]. On the eastern side, the large proportion of trees may be related to a man-made drainage ditch from approximately 80 years ago (linear feature from north to south in Figure 5), which influences the hydrology and vegetation composition in this area [31]. In addition, the treed areas classified in our study were consistent with those previously mapped by [30] using Landsat imagery and leaf area index (LAI) models. Further validation of our preliminary classification for Mer Bleue would require the use of very high-resolution photogrammetry, as measured by [21] for a 10-hectare section of Mer Bleue, in order to carry out an adequate classification accuracy assessment.

Estimation of the spatial distribution of maximum gross photosynthesis (PGmax) for hummocks was performed during the peak of the growing season (23 June). Our results show that values of 8–12 $\mu\text{mol m}^{-2} \text{s}^{-1}$ are predominant at Mer Bleue during this time, although it is important to note that the empirical model relating PGmax and NDVI has a coefficient of determination of 0.6, and therefore our results of PGmax for hummocks are approximate. The current relationship between NDVI and PGmax is also dependent on the three lower data points (NDVI < 0.6), a limitation of the available data for assessing PGmax at the landscape level. More plot-level measurements combined with field spectroscopy focusing on both vascular plants and mosses are recommended at MBCA to improve the models we use here. Nevertheless, given the high proportion of hummocks (51.2%) that are dominated by green broadleaf vegetation in June, we identified spatial differences in PGmax throughout the bog. For instance, the central part of Mer Bleue has a larger proportion of lower PGmax values (4–8 $\mu\text{mol m}^{-2} \text{s}^{-1}$), which might be explained by higher gravimetric water content in this area of the bog (Figure 8). Overall, a reduction of photosynthetic activity in waterlogged areas is expected for vascular plants due to a decrease in O₂ and lower stomatal aperture [41], even under conditions where plants are adapted to wet conditions.

Remote-sensing studies have shown the utility of the SWIR region (0.9–2.5 μm) for assessing water content in vegetation and the acrotelm of bog ecosystems (see [42] for a review). Based on the NDWI₁₆₄₀ index, we identified temporal patterns of near-surface water content for hollows and hummocks. High near-surface water content was found in November 2015 (prior to snowfall), with decreasing values from April to May (spring) and a significant increase for June 2016 (Figure 8), following typical

phenological patterns associated with the greening up of the vegetation at Mer Bleue [25]. Moreover, as expected, significantly higher $NDWI_{1640}$ values were found for hollows than for hummocks for all periods. *Sphagnum* species are specially adapted bryophytes, for which water is supplied to their capitula from rainfall or via capillary movement from the water table [14], which allows them to accumulate more near-surface water than vascular plants. *Sphagnum* leaves are only one cell thick and in direct contact with the water in their environment [10]. It has also been shown that vascular plants have higher reflectance in the SWIR region as they have lower water content [18]. The relatively high and equivalent mean values of $NDWI_{1640}$ (between HU and HO) from 23 June might be explained by the solar azimuth angle (SAA) relative to the heading of the flight line being diagonal to the SASI's field of view. Kalacska et al. 2018 (in this issue) describe how certain ranges of SAA might introduce errors into the resulting biophysical models. Moreover, it is important to mention that our *t*-test results (Table 3) are limited given the large sample size we used to compare HO and HU for each date [43]. In this case, we compared the probability density functions for the 5 dates for HU and HO to support our findings (Appendix A). Further statistical analysis could enhance the understanding of the temporal patterns we found for HO and HU; however, this is beyond the scope of this study.

Similar to our empirical model for PGmax, our GWC is derived for the different days with a linear model based on $NDWI_{1640}$ [17], which explains 85% of the total variance (up to 1600% GWC). Our results capture the temporal variation of GWC and we also found significant differences in GWC between dates (Table 4, Figure 9B). Due to the large sample size ($n > 11$ million) it is important to interpret the significance values for the statistical tests with caution [43]; the confidence intervals may be more informative in terms of the differences in the mean values than the actual *p* value (Table 3). For instance, Figure 9B compares the probability density function (PDF) for GWC for each date, which provides a visual assessment on the differences in GWC between dates. Spatially, we identified that a central belt of Mer Bleue has GWC values $> 1000\%$ (Figure 8) and that more GWC temporal variations are found not only in the three fingers in the western sector, but also some sections of the eastern sector. The area comprising the top finger corresponds to a well-studied section of Mer Bleue. Temporal variations in GWC here might be related to an identified domed shape of this section, with peat depths varying from 5–6 m in the middle and decreasing to about 2 m toward the edges (as described in [32]). This section of Mer Bleue is also close to a beaver pond and transition areas are located between the pond and the bog area.

CO_2 uptake efficiency in hollows was inferred from an optimum curve for *Sphagnum* species [13]; therefore, our results are an approximation for Mer Bleue, for which further field validation would be required. Water availability is very important for *Sphagnum* mosses because they lack a mechanism to actively control water loss; therefore, water-table level (capillary transportation), density of capitula (e.g., species in hummock vs hollow), and surface water availability influence C assimilation [10,14]. Our results confirm that the GWC for the central part of Mer Bleue are within the optimal-to-wet conditions for all periods, which might be an indication of the water table closer to the surface in this area. Conversely, it is important to note that the upper and lower fingers in the study area show a higher variation of CO_2 uptake efficiency over time, especially during green-up (11 and 24 May sampling dates) where suboptimal CO_2 uptake efficiency values are predominant with some areas falling into the water-deficit category (Figure 10). This is an important finding because the effects of climate change scenarios for northern peatlands are still under discussion [44–46] and both water availability and temperature changes, in addition to other ecosystem variables [47], could have major impacts on the capability of *Sphagnum* mosses to effectively uptake and store C. Furthermore, water-table position in the north-west part of Mer Bleue is highly variable within and across years [48], and continuous monitoring of this section both with in situ measurements and using hyperspectral remote-sensing tools could better inform the actual response of mosses to deficits in water availability.

5. Conclusions

Studies of peatland ecosystem-level photosynthesis (e.g., CO₂ uptake and respiration) are important in order to understand the response of these ecosystems to climate change in the long term (sink vs. source) and to evaluate short-term (e.g., seasonal) responses of mosses and vascular plants to water availability. Because of the low accessibility to peatland areas (e.g., [49]) and their fragile structure, integrating in situ empirical models with remotely sensed data acquired at adequate spatial, spectral and temporal scales might be the only way to understand patterns and processes at larger spatial scales (>100 hectares). Our study offers a methodological approach that combines empirical models based on in situ characterization of peatland microforms with high spatial resolution hyperspectral imagery. However, even using remotely sensed data at the necessary scales, we relied significantly on empirical models that might not cover the full range of variation in this peatland area. Therefore, our results require further validation either by increasing ground sampling to other areas at Mer Bleue, or by continually acquiring hyperspectral data for multiple areas over a longer period of time in order to assess the consistency of our results. Moreover, as Mer Bleue is considered an Arctic Surrogate Simulation Site for Sentinel-2 and Landsat-8 satellite data product validation and a Committee for Earth Observation Satellites (CEOS) Land Product Validation (LPV) Subgroup supersite, future research will continue in order to evaluate the use of these or similar space-borne systems in assessing ecosystem-level carbon dynamics.

An important aspect not fully addressed in this paper is the effect of cross-track illumination artifacts when using airborne hyperspectral mosaics. Observable cross-track illumination artifacts were identified in certain flight lines (i.e., when the ground track differed from the solar azimuth angle). After the application of a simple removal of the artifacts, minor issues remained. We considered them to be minimal in their effect on the overall results as they accounted only for very specific and narrow sections of the full mosaic (e.g., overlap between adjacent lines). However, further analysis is needed to fully correct for these artifacts in the products derived from airborne hyperspectral imagery.

We identified spatial differences in ecosystem gross photosynthesis across the entire area of the bog. Furthermore, for the hollow class, the temporal and spatial variation of GWC and CO₂ uptake efficiency is highly variable. Because a substantial part of the field research at Mer Bleue has focused on the research boardwalk area, which covers approximately 10 ha, our results shed new light on other zones of interest where further studies are recommended to validate the patterns and trends obtained from the imagery. For example, the eastern sector modified by the drainage ditch could be used as a model for remote-sensing studies of drained peatlands (e.g., agriculture, harvesting) in order to understand the impact of land-use cover change on carbon uptake. Finally, our findings could also be integrated into net ecosystem exchange models where the proportion of microforms in a landscape play a fundamental role.

Acknowledgments: We acknowledge the funding provided by the European Space Agency (ESA) Sensor Performance, Products and Algorithms (SPPA) element of the Earth Observation ground segment (to NRC). This work was also supported by the Natural Sciences and Engineering Research Council of Canada (NSERC) and Canada Foundation for Innovation (CFI) (to Kalacska). We thank the National Capital Commission (NCC) for access to Mer Bleue. We also thank Mike Dalva for logistics support at Mer Bleue, Oliver Lucanus for the UAV photographs, and Julie de Gea for spectral data collection. We would like to express our appreciation to DRDC-Valcartier for the loan of the CASI instrument.

Author Contributions: J.P.A.-M. and M.K. conceived, designed and performed the data analysis; J.P.A.-M., M.K. and T.R.M. wrote the manuscript, R.J.S. and G.I. collected the imagery; R.J.S., M.K., G.I. and D.I. preprocessed the imagery; S.J. collected and processed the PGmax data and PAI data; T.R.M. and N.T.R. assisted in the data analysis and interpretation, G.L. procured CASI/SASI sensors, all authors reviewed and improved the overall manuscript.

Conflicts of Interest: The authors declare no conflict of interest.

Appendix A

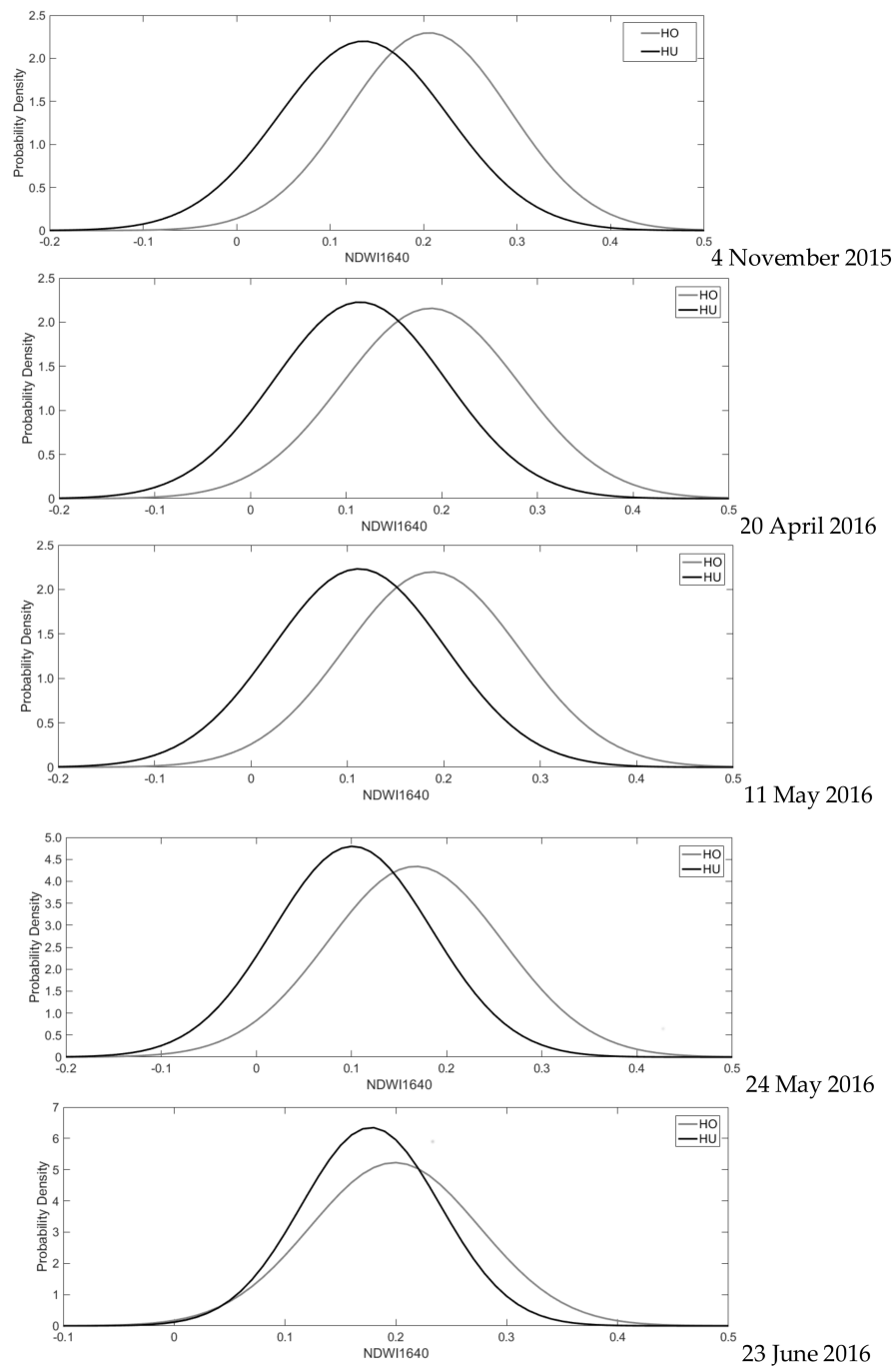


Figure A1. Probability density functions (PDF) comparing hollow (HO) v hummocks (HU) near surface water content based on the NDWI₁₆₄₀.

Table A1. Normal probability density function parameters for the hummock (HU) and hollow (HO) GWC comparison.

	μ (Mean)	μ -ci (95% Confidence Interval)	σ (Standard Deviation)	σ -ci (95% Confidence Interval)
4 November 2015				
HO	0.206	0.20555, 0.20577	0.087	0.08676, 0.08692
HU	0.136	0.13559, 0.13571	0.091	0.09066, 0.09074
20 April 2016				
HO	0.188	0.18829, 0.18852	0.092	0.09239, 0.09256
HU	0.114	0.11438, 0.11449	0.090	0.08951, 0.08959
11 May 2016				
HO	0.188	0.18764, 0.18786	0.091	0.09072, 0.09088
HU	0.112	0.11178, 0.11190	0.089	0.08933, 0.08941
24 May 2016				
HO	0.167	0.16712, 0.16735	0.092	0.09186, 0.09203
HU	0.101	0.10097, 0.10108	0.083	0.08315, 0.08323
23 June 2016				
HO	0.199	0.19888, 0.19908	0.076	0.07628, 0.07641
HU	0.177	0.17741, 0.17749	0.063	0.06280, 0.06286

References

- Loisel, J.; Yu, Z.; Beilman, D.W.; Camill, P.; Alm, J.; Amesbury, M.J.; Anderson, D.; Andersson, S.; Bochicchio, C.; Barber, K.; et al. A database and synthesis of northern peatland soil properties and Holocene carbon and nitrogen accumulation. *Holocene* **2014**, *24*, 1028–1042. [[CrossRef](#)]
- Eppinga, M.B.; Rietkerk, M.; Borren, W.; Lapshina, E.D.; Bleuten, W.; Wassen, M.J. Regular Surface Patterning of Peatlands: Confronting Theory with Field Data. *Ecosystems* **2008**, *11*, 520–536. [[CrossRef](#)]
- Belyea, L.R.; Clymo, R.S. Feedback control of the rate of peat formation. *Proc. R. Soc. Lond. B Biol. Sci.* **2001**, *268*, 1315–1321. [[CrossRef](#)] [[PubMed](#)]
- Lai, D.Y.F.; Roulet, N.T.; Humphreys, E.R.; Moore, T.R.; Dalva, M. The effect of atmospheric turbulence and chamber deployment period on autochamber CO₂ and CH₄ flux measurements in an ombrotrophic peatland. *Biogeosciences* **2012**, *9*, 3305–3322. [[CrossRef](#)]
- Lafleur, P.M.; Hember, R.A.; Admiral, S.W.; Roulet, N.T. Annual and seasonal variability in evapotranspiration and water table at a shrub-covered bog in southern Ontario, Canada. *Hydrol. Process.* **2005**, *19*, 3533–3550. [[CrossRef](#)]
- Moore, T.; Basiliko, N. Decomposition in Boreal Peatlands. In *Boreal Peatland Ecosystems*; Wieder, R.K., Vitt, D.H., Eds.; Springer: Berlin/Heidelberg, Germany, 2006; pp. 125–143.
- Murphy, M.T.; Moore, T.R. Linking root production to aboveground plant characteristics and water table in a temperate bog. *Plant Soil* **2010**, *336*, 219–231. [[CrossRef](#)]
- Talbot, J.; Roulet, N.T.; Sonnentag, O.; Moore, T.R. Increases in aboveground biomass and leaf area 85 years after drainage in a bog. *Botany* **2014**, *92*, 713–721. [[CrossRef](#)]
- Moore, T.R.; Bubier, J.L.; Bledzki, L. Litter Decomposition in Temperate Peatland Ecosystems: The Effect of Substrate and Site. *Ecosystems* **2007**, *10*, 949–963. [[CrossRef](#)]
- Rydin, H.; Jeglum, J.K. *The Biology of Peatlands*; Oxford University Press: Oxford, UK, 2013.
- Titus, J.E.; Wagner, D.J. Carbon Balance for Two Sphagnum Mosses: Water Balance Resolves a Physiological Paradox. *Ecology* **1984**, *65*, 1765–1774. [[CrossRef](#)]
- Titus, J.E.; Wagner, D.J.; Stephens, M.D. Contrasting Water Relations of Photosynthesis for Two Sphagnum Mosses. *Ecology* **1983**, *64*, 1109–1115. [[CrossRef](#)]
- Schipperges, B.; Rydin, H. Response of photosynthesis of *Sphagnum* species from contrasting microhabitats to tissue water content and repeated desiccation. *New Phytol.* **1998**, *140*, 677–684. [[CrossRef](#)]

14. Harris, A.; Bryant, R.G.; Baird, A.J. Mapping the effects of water stress on *Sphagnum*: Preliminary observations using airborne remote sensing. *Remote Sens. Environ.* **2006**, *100*, 363–378. [[CrossRef](#)]
15. Banskota, A.; Falkowski, M.J.; Smith, A.M.S.; Kane, E.S.; Meingast, K.M.; Bourgeau-Chavez, L.L.; Miller, M.E.; French, N.H. Continuous Wavelet Analysis for Spectroscopic Determination of Subsurface Moisture and Water-Table Height in Northern Peatland Ecosystems. *IEEE Trans. Geosci. Remote Sens.* **2017**, *55*, 1526–1536. [[CrossRef](#)]
16. Harris, A.; Bryant, R.G. A multi-scale remote sensing approach for monitoring northern peatland hydrology: Present possibilities and future challenges. *J. Environ. Manag.* **2009**, *90*, 2178–2188. [[CrossRef](#)] [[PubMed](#)]
17. Lalonde, M. The Hyperspectral Determination of Sphagnum Water Content in a Bog. Master's Thesis, McGill University, Montreal, QC, Canada, 2013.
18. Bubier, J.L.; Rock, B.N.; Crill, P.M. Spectral reflectance measurements of boreal wetland and forest mosses. *J. Geophys. Res. Atmos.* **1997**, *102*, 29483–29494. [[CrossRef](#)]
19. Vogelmann, J.E.; Moss, D.M. Spectral reflectance measurements in the genus *Sphagnum*. *Remote Sens. Environ.* **1993**, *45*, 273–279. [[CrossRef](#)]
20. Meingast, K.M.; Falkowski, M.J.; Kane, E.S.; Potvin, L.R.; Benscoter, B.W.; Smith, A.M.S.; Bourgeau-Chavez, L.L.; Miller, M.E. Spectral detection of near-surface moisture content and water-table position in northern peatland ecosystems. *Remote Sens. Environ.* **2014**, *152*, 536–546. [[CrossRef](#)]
21. Arroyo-Mora, J.P.; Kalacska, M.; Lucanus, O.; Soffer, R.J.; Leblanc, G. Spectro-Spatial Relationship between UAV Derived High Resolution DEM and SWIR Hyperspectral Data: Application to an Ombrotrophic Peatland. In Proceedings of the SPIE, Warsaw, Poland, 11–14 September 2017.
22. Larmola, T.; Bubier, J.L.; Kobyljanec, C.; Basiliko, N.; Juutinen, S.; Humphreys, E.; Preston, M.; Moore, T.R. Vegetation feedbacks of nutrient addition lead to a weaker carbon sink in an ombrotrophic bog. *Glob. Chang. Biol.* **2013**, *19*, 3729–3739. [[CrossRef](#)] [[PubMed](#)]
23. Kalacska, M.; Arroyo-Mora, J.P.; Soffer, R.; Leblanc, G. Quality Control Assessment of the Mission Airborne Carbon 13 (MAC-13) Hyperspectral Imagery from Costa Rica. *Can. J. Remote Sens.* **2016**, *42*, 85–105. [[CrossRef](#)]
24. Soffer, R.; Arroyo-Mora, J.P.; Kalacska, M.; Ifimov, G.; White, P.H.; Leblanc, S.; Nazarenko, D.; Leblanc, G. MBASSS Landsat 8 Data Product Validation Project—Final Report; National Research Council: Ottawa, ON, Canada, 2017.
25. Arroyo-Mora, J.P.; Kalacska, M.; Soffer, R.J.; Ifimov, G.; Leblanc, G.; Schaaf, E.S.; Lucanus, O. Phenospectral dynamics of vegetation physiognomies at different spatial and spectral scales at the Mer Bleue ombrotrophic peatland. *Remote Sens. Environ.* **2018**. Under Review.
26. Leifeld, J.; Menichetti, L. The underappreciated potential of peatlands in global climate change mitigation strategies. *Nat. Commun.* **2018**, *9*, 1071. [[CrossRef](#)] [[PubMed](#)]
27. Lafleur, P.M.; Roulet, N.T.; Admiral, S.W. Annual cycle of CO₂ exchange at a bog peatland. *J. Geophys. Res. Atmos.* **2001**, *106*, 3071–3081. [[CrossRef](#)]
28. Waddington, J.M.; Quinton, W.L.; Price, J.S.; Lafleur, P.M. Advances in Canadian Peatland Hydrology, 2003–2007. *Can. Water Resour. J.* **2009**, *34*, 139–148. [[CrossRef](#)]
29. Moore, T.R.; Bubier, J.L.; Frolking, S.E.; Lafleur, P.M.; Roulet, N.T. Plant biomass and production and CO₂ exchange in an ombrotrophic bog. *J. Ecol.* **2002**, *90*, 25–36. [[CrossRef](#)]
30. Sonntag, O.; Chen, J.M.; Roberts, D.A.; Talbot, J.; Halligan, K.Q.; Govind, A. Mapping tree and shrub leaf area indices in an ombrotrophic peatland through multiple endmember spectral unmixing. *Remote Sens. Environ.* **2007**, *109*, 342–360. [[CrossRef](#)]
31. Bubier, J.L.; Moore, T.R.; Crosby, G. Fine-scale vegetation distribution in a cool temperate peatland. *Can. J. Bot.* **2006**, *84*, 910–923. [[CrossRef](#)]
32. Lafleur, P.M.; Roulet, N.T.; Bubier, J.L.; Frolking, S.; Moore, T.R. Interannual variability in the peatland-atmosphere carbon dioxide exchange at an ombrotrophic bog. *Glob. Biogeochem. Cycles* **2003**, *17*, 13. [[CrossRef](#)]
33. Collings, S.; Caccetta, P.; Campbell, N.; Wu, X. Techniques for BRDF Correction of Hyperspectral Mosaics. *IEEE Trans. Geosci. Remote Sens.* **2010**, *48*, 3733–3746. [[CrossRef](#)]
34. Peñuelas, J.; Filella, I.; Gamon, J.A. Assessment of photosynthetic radiation-use efficiency with spectral reflectance. *New Phytol.* **1995**, *131*, 291–296. [[CrossRef](#)]

35. Gamon, J.A.; Serrano, L.; Surfus, J.S. The photochemical reflectance index: An optical indicator of photosynthetic radiation use efficiency across species, functional types, and nutrient levels. *Oecologia* **1997**, *112*, 492–501. [[CrossRef](#)] [[PubMed](#)]
36. Wilson, P. The Relationship Among Micro-Topographic Variation, Water Table Depth and Biogeochemistry in an Ombrotrophic Bog. Master's Thesis, McGill University, Montreal, QC, Canada, 2012.
37. Juutinen, S.; Bubier, J.L.; Moore, T.R. Responses of Vegetation and Ecosystem CO₂ Exchange to 9 Years of Nutrient Addition at Mer Bleue Bog. *Ecosystems* **2010**, *13*, 874–887. [[CrossRef](#)]
38. Gao, B.-. C NDWI—A normalized difference water index for remote sensing of vegetation liquid water from space. *Remote Sens. Environ.* **1996**, *58*, 257–266. [[CrossRef](#)]
39. Rietkerk, M.; Dekker, S.C.; de Ruiter, P.C.; van de Koppel, J. Self-Organized Patchiness and Catastrophic Shifts in Ecosystems. *Science* **2004**, *305*, 1926–1929. [[CrossRef](#)] [[PubMed](#)]
40. Lehmann, J.; Münchberger, W.; Knoth, C.; Blodau, C.; Nieberding, F.; Prinz, T.; Pancotto, V.; Kleinebecker, T. High-Resolution Classification of South Patagonian Peat Bog Microforms Reveals Potential Gaps in Up-Scaled CH₄ Fluxes by use of Unmanned Aerial System (UAS) and CIR Imagery. *Remote Sens.* **2016**, *8*, 173. [[CrossRef](#)]
41. Parent, C.; Capelli, N.; Audrey, B.; Crevêcoeur, M.; Dat, J. *An Overview of Plant Responses to Soil Waterlogging*; Global Science Books Ltd.: Sussex, UK, 2008; Volume 2.
42. Lees, K.J.; Quaife, T.; Artz, R.R.E.; Khomik, M.; Clark, J.M. Potential for using remote sensing to estimate carbon fluxes across northern peatlands—A review. *Sci. Total Environ.* **2018**, *615*, 857–874. [[CrossRef](#)] [[PubMed](#)]
43. Lin, M.; Jr, H.C.L.; Shmueli, G. Research Commentary—Too Big to Fail: Large Samples and the *p*-Value Problem. *Inf. Syst. Res.* **2013**, *24*, 906–917. [[CrossRef](#)]
44. Frolking, S.; Talbot, J.; Jones, M.C.; Treat, C.C.; Kauffman, J.B.; Tuittila, E.-S.; Roulet, N. Peatlands in the Earth's 21st century climate system. *Environ. Rev.* **2011**, *19*, 371–396. [[CrossRef](#)]
45. Wu, J.; Roulet, N.T. Climate change reduces the capacity of northern peatlands to absorb the atmospheric carbon dioxide: The different responses of bogs and fens. *Glob. Biogeochem. Cycles* **2014**, *28*, 1005–1024. [[CrossRef](#)]
46. Oke, T.A.; Hager, H.A. Assessing environmental attributes and effects of climate change on *Sphagnum* peatland distributions in North America using single- and multi-species models. *PLoS ONE* **2017**, *12*, e0175978. [[CrossRef](#)] [[PubMed](#)]
47. Waddington, J.M.; Morris, P.J.; Kettridge, N.; Granath, G.; Thompson, D.K.; Moore, P.A. Hydrological feedbacks in northern peatlands. *Ecohydrology* **2015**, *8*, 113–127. [[CrossRef](#)]
48. Malhotra, A.; Roulet, N.T.; Wilson, P.; Giroux-Bougard, X.; Harris, L.I. Ecohydrological feedbacks in peatlands: An empirical test of the relationship among vegetation, microtopography and water table. *Ecohydrology* **2016**, *9*, 1346–1357. [[CrossRef](#)]
49. Tarnocai, C.; Kettles, I.M.; Lacelle, B. *Peatlands of Canada Database*; Digital Database; Research Branch, Agriculture and Agri-Food Canada: Ottawa, ON, Canada, 2005.



© 2018 by the authors. Licensee MDPI, Basel, Switzerland. This article is an open access article distributed under the terms and conditions of the Creative Commons Attribution (CC BY) license (<http://creativecommons.org/licenses/by/4.0/>).